DATA ANALYSIS OF MARKARIAN 421 OBSERVED BY THE HIGH ENERGY STEREOSCOPIC SYSTEM (H.E.S.S.) IN JANUARY 2017

A RESEARCH THESIS SUBMITTED IN PARTIAL FULFILMENT

OF THE REQUIREMENTS FOR THE DEGREE OF

MASTER OF SCIENCE IN PHYSICS

OF

THE UNIVERSITY OF NAMIBIA

BY

TAUNO TUHAFENI KAMUDULUNGE NANGHONGA

200970992

April 2021

Main Supervisor: Dr M. Backes

(University of Namibia, Department of Physics)

Co-supervisor: Mr I.D. Davids

(University of Namibia, Department of Physics)

Contents

1. Introduction 1

1.1 Background of the Study 1

2. Literature Review 5

2.2 Gamma-ray blazars 7

2.3 Markarian 421 9

Instruments and methods 15

3.1 The H.E.S.S. telescopes 15

3.1.1 H.E.S.S. site 15

3.1.2 The layout and mirror systems 16

3.1.3 The H.E.S.S. Upgraded Cameras 18

3.1.4 Status of the Upgrade 19

3.2 The analysis software 22

3.2.1 The H.E.S.S. Analysis Package 22

3.2.2 Installing HAP 23

3.2.3 Cut Configuration Files 25

3.2.4 Using HAP-a step-by -step analysis 25

3.2.5 Obtaining a list of runs 26

3.2.6 Making a configuration file 26

4.1 Running HAP 28

4.2 Looking at the output 28

4.3 Producing output plots 29

4.4 Paris step-by-step analysis 29

4.4.1 The analysis commands 29

4.4.2 Viewing at the output 30

4.5. The ring background method 37

4.6. The reflected background method 40

4.7. The light curve 41

Conclusion 44

References 46

Table of Figures

Figure 2. 1 The sky map of Markarian 421 observed by H.E.S.S. after the H.E.S.S. phase I camera upgrade in 2017 [2]. The colour bar indicates the statistical significance of the detection at the various sky positions. A large significance of gamma-ray detection can be seen at the position of Mrk 421, near the centre of the image. 6

Figure 2.2 The SED of another AGN, 3C 279. It shows synchrotron radiation responsible for the low energy bump and the inverse-Compton emission responsible for the second high-energy bump. This double feature is very characteristic of blazars. 8

Figure 2.4 The long-term light curve of Mark 421 [9]. 11

Figure 2.5 Comments to the observed flux of April 2004 flare with the photohadronic model using two different EBL models are shown. It is also compared with the power law with exponential cut-off without EBL correction fit and with the multi-zone leptonic fit. The multi-zone leptonic model accounts for the attenuation of the very high-energy gamma-rays by the diffuse infrared background. The intrinsic fluxes for the two EBL models are also shown [12]. 13

Figure 2.6 Fit to the observed flux of 2010 flare by H.E.S.S. using the photohadronic model and the EBL correction to it by EBL-D and EBL-I are shown. The corresponding intrinsic fluxes are also given [12]. 14

Figure 3.1 A picture of the H.E.S.S. site. Credit: H.E.S.S.ecap.nat.fau.de 16

Figure 3.2 A picture of the lid CCD placed at the centre of each telescope. Credit: H.E.S.S. uni-tuebingen.de 17

Figure 3.3 Left: The camera of a H.E.S.S. I telescope. Right: A close-up view of the H.E.S.S. II camera showing the photomultipliers and Winston cones. credit: H.E.S.S. Gamma ray telescope in Namibia. Hermanus astronomy.co.za 17

Figure 3.4 One of the H.E.S.S. cameras in its shelter [23]. It has 960 photomultiplier pixels of size 0.16°, resulting in a 5° field of view. The electronics with 1 GHz analog sampling rate are entirely contained in the camera body. 18

Figure 3.6 Testing setups at DESY (Zeuthen) – CopyCam (top) and test bench with pulse generators (bottom) [24]. 21

Figure 4.1 Top: Energy spectrum described by a power-law with spectral index 3.22± 0.27 decreasing in flux as the energy increases. Bottom: Reconstructed energy. 32

Figure 4.2 Top: Energy spectrum described by a power-law with exponential cut-off is observed to have the spectral index 0.80 ±1.61 with the exponential cut at 2.53 ±1.70 TeV energy. Bottom: Reconstructed energy. 33

Figure 4.3 Left: Sky map showing the source position. Middle: the significance map. And right: significance distribution with the mean value 1.22+-0.01. 38

Figure 4. 4 The $\theta 2$ distribution is often used to display the excess of gamma rays from the position of the source, especially for point like sources. As we can see from this figure, the distribution follows the shape of the (point spread function) PSF, demonstrating that the instrument (H.E.S.S.) response function is processed correctly by Parish analysis. 39

Figure 4.5 The night-by-night light curve that shows the average flux per night as a function of MJD. 42

Figure 4.6 The run-by-run light curve that shows the brightness recorded at different energies for each observed run. 42

List of Abbreviations

AGN	**A**ctive **G**alactic **N**uclei
ASICs	**A**pplication-**s**pecific **I**ntegrated **C**ircuits
AAVSO	**A**merican **A**ssociation of **V**ariable **S**tar **O**bservers
CT	**C**herenkov **T**elescope
CXB	**C**osmic **X**-ray **B**ackground
CCD	**C**harge **C**oupled **D**evice
CVS	**C**oncurrent **V**ersion **S**ystem
CRs	**C**osmic **R**ays
DEC	**Dec**lination
DST	**D**ata **S**ets (H.E.S.S. Processed Event Data)
EBL	**E**xtragalactic **B**ackground **L**ight
EPWL	**E**xponential **p**ower-**l**aw
FPGA	**F**ield-**P**rogrammable **G**ate **A**rray
FIFO	**F**irst-**I**n,-**F**irst-**O**ut
FSRQ	**F**lat **S**pectrum **R**adio **Q**uasar
FoV	**F**ield **o**f **V**iew
HAWC	**H**igh-**A**ltitude **W**ater **C**herenkov (Detector)
H.E.S.S.	**H**igh **E**nergy **S**tereoscopic **S**ystem

HBL	**H**igh-frequency peaked **BL** **L**acs
HV	**H**igh **v**oltage
HG	**H**igh **g**ain
HAP	**H**.E.S.S. **A**nalysis **P**ackage
IACTs	**I**maging **A**tmospheric **C**herenkov **T**elescope
IRFs	**I**nstrument **R**esponse **F**unctions
LEDs	**L**ight **e**mitting **d**iodes
LG	**L**ow **g**ain
MJD	**M**odified **J**ulian **D**ate
Mrk 421	**Mrk**arian **421**
PMTs	**P**hoto**m**ultiplier **T**ubes
PWL	**P**ower-**l**aw
RXTE	**R**ossi **X**-ray **T**iming **E**xplorer
SSC	**S**ynchrotron **S**elf-**C**ompton
SMBH	**S**uper**m**assive **b**lack **h**ole
SED	**S**pectral **e**nergy **d**istribution
TeV	**T**era-**e**lectron **V**olt
TMVA	**T**oolkit for **M**ultivariable **D**ata **A**nalysis
VHE	**V**ery **H**igh **E**nergy

VERITAS **V**ery **E**nergetic **R**adiation **I**maging **T**elescope **A**rray **S**ystem

Acknowledgements

I give thanks to God for my health, my strength, my wisdom, my understanding and my knowledge.

I wish to thank Dr. M Backes, my supervisor, for his support and guidance during the project. It is always nice working with him.

With great pleasure, I thank Mr. ID Davids, my co-supervisor, for his effort and guidance during the writing of my project.

I would also like to thank Mr. J Shapopi, my course-mate, for his assistance during my data analysis with the Paris analysis software.

Finally, I will thank Mr. GN Festus, my pastor, for his prayers during my entire course work and, also, I thank my wife for the encouragement during my course work.

Dedication

I dedicate this work to **God** for the strength and blessings he has given me. This project was completed by his grace. To my parents and siblings, I cannot thank you enough for your great support during this project.

To my wonderful course-mates and friends, I say thank you for your assistance and advices. You made it happen!

Declarations

I, TAUNO TUHAFENI KAMUDULUNGE NANGHONGA, certify that this work, "DATA ANALYSIS OF MARKARIAN 421 OBSERVED BY THE HIGH ENERGY STEREOSCOPIC SYSTEM (H.E.S.S.) IN JANUARY 2017" is truly my work carried out under the supervision of Dr Michael Backes.

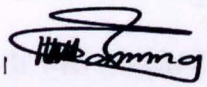

Mr TTK NANNGHONGA
STUDENT
DEPARTMENT OF PHYSICS
UNIVERSITY OF NAMIBIA

Abstract

The investigation of Active Galactic Nuclei (AGN) is one of the most important areas of contemporary astrophysics. In general, the term AGN refers to the existence of energetic phenomena in the nucleus (central region) of a galaxy which cannot be attributed to the stars in that galaxy. Blazars are AGN that are viewed from Earth head-on, and that exhibits extra-ordinary large variability on time scales sometimes less than hours, often displaying highly irregular and flare-like behavior. Among blazars detected at very-high energies, Markarian 421 is one of the brightest and best studied. It was detected by the High Energy Stereoscopic System (H.E.S.S.) in January 2017 during a flaring state. H.E.S.S. is a γ-ray astronomy array of telescopes, located in Namibia, near the Gamsberg mountain, an area known for its excellent astronomical observational conditions.

The observational data from the H.E.S.S. experiment was used in this case to obtain and explain the light curve and the energy spectrum for the seven data sets recorded in January 2017. With the Model++ (also called Paris Analysis) standard cuts analysis, an excess of 115.5 γ rays, for $N_{on} = 122$ on-source and $N_{off} = 108$ off-source events are detected at the 19.9σ significance level. We have observed that the energy spectrum, can be well described by a power-law with spectral index 3.22 ± 0.27 decreasing in flux as the energy increases. Fitting the observed Spectral Energy Distribution (SED) with a power-law with exponential cut-off is observed to have the spectral index 0.80 ± 1.61 with the exponential cut at 2.53 ± 1.70 TeV photon energy.

As for the light curves (the radiation flux as a function of time), the scarcity of the data could not reveal any meaningful variability pattern to be deduced from these January 2017 observations.

Chapter 1

1. Introduction

1.1 Background of the Study

The discovery of cosmic rays started with Victor Hess when he first took off for his legendary balloon flight in 1912, but he certainly did not imagine that almost 100 years later a whole branch of physics occupied by thousands of physicists worldwide would have evolved from it. In recent years, the field of γ-ray astrophysics has rapidly developed. This is due to the list of ground-based Imaging Atmospheric Cherenkov Telescopes (IACTs) and space-based instruments that are now operational. Furthermore, the currently operating ground missions committed to γ-ray astrophysics include the High Energy Stereoscopic System (H.E.S.S.), the Very Energetic Radiation Imaging Telescope Array System (VERITAS), and the Major Atmospheric Gamma Imaging Cherenkov (MAGIC) telescopes that operate in the 100 GeV – 100 TeV photon energy band.

The future Cherenkov Telescope Array (CTA) will be 10 times more sensitive than H.E.S.S. The launch of the Fermi Large Area Telescope (*Fermi*-LAT) in 2008, operating at 20 MeV – 300 GeV, has led to many discoveries, including the detection of γ rays from various sources [1]. *Fermi*-LAT is the main instrument on-board the Fermi Gamma-ray Space Telescope (formerly called GLAST) which is a γ-ray satellite orbiting the Earth on a low orbit of 550 km altitude.

This study is focused on γ-ray data analysis of Mrk 421 observed by H.E.S.S. in January of the year 2017. These observations were triggered by a flaring state of the source detected by the High-Altitude Water Cherenkov (HAWC) detector [2].

H.E.S.S. is a system of IACTs that observes cosmic γ rays in the energy range from tens of GeV to tens of TeV. The instrument allows the exploration of γ-ray sources with intensities at a level of few thousandths of the flux of the Crab Nebula (the brightest steady source of γ rays in the sky) [17].

H.E.S.S. is located in Namibia, near the Gamsberg Mountain, an area well known for its excellent astronomical observing conditions. The system has been operating with the first phase of the full array of telescopes since 2004. With the system going over into its second phase (with an additional large telescope added) in 2012. On top of that, the system has undergone some upgrades (especially camera-related) during the recent years.

Despite the development of detectors in γ-ray astronomy, there are still many unanswered questions in the field, some of which will greatly impact our understanding of the Universe when finally resolved. For example, there is no definite answer to where and how are the extragalactic cosmic rays are produced and accelerated. Other questions include the quest for identifying the underlying energy source of highly energetic phenomena in the Universe. As will be mentioned herein, there are currently various schools of thought towards this and other open questions in the field.

The core research goal with this work is to obtain and explain the light curve and the spectral energy distribution (SED) of very-high energy γ rays from the blazar Mrk 421. The light curve can typically give insight into the temporal variability scale, which in turn can be used to put estimates on the size of the regions of the source from which γ

rays are emitted. On the other hand, studies of SEDs can typically be used to characterize astronomical sources. In an attempt, to exploit these features, the January 2017 γ-ray data from H.E.S.S. of Mrk 421 has been analysed to reproduce the emission spectrum and temporal evolution of this source.

In summary, the main objectives were to:

(a) obtain and explain the flux as a function of time (i.e. light curve),

(b) obtain and explain the γ-ray flux as a function of energy (i.e. the SED).

On the national level, this research contributes to improving the human capital development by increasing the number of Namibians participating in research with H.E.S.S. leading to improved international collaboration.

For this thesis, only January 2017 γ-ray data of Mrk 421 will be analysed, utilizing the new camera system commissioned in 2017. We single out and concentrate on this data set because, at that time, an exceptionally bright flare of the source was observed and reported by HAWC. This HAWC detection alerted and triggered the H.E.S.S. Target of Opportunity (ToO) observations, and these observations produced the dataset in question. HAWC is a particle detector using water tanks at a high altitude in which the particles produced by incident γ rays in turn produce Cherenkov radiation.

With this work we can produce the SED at least in the TeV regime where H.E.S.S. is sensitive, and this can be used to compare with the predictions from physical models that are based on γ-ray emissions due to Synchrotron Self-Compton and inverse Compton radiation models.

This thesis consists of five chapters. Chapter one discusses the background of the study, and the problem statement with its objectives and significance. It also includes the aspects of the limitation and delimitation of the study. The second chapter gives the literature review which includes the basics of cosmic rays and their possible origins, and discusses blazars (a special class of active galaxies), provides more discussion on the source Mrk 421 and its flaring history from previous studies. The third chapter explains the instrument and methods used and provides the description of the cameras of the H.E.S.S. telescopes. It also talks about the upgraded cameras of the H.E.S.S. telescopes and lastly, the analysis software used in analysing data. The analysis discussion outlines the step-by-step procedure as described the analysis configurations of the software. Chapter four gives the output and results of the analysis, and chapter five gives the discussion and interpretation thereof.

Chapter 2

2. Literature Review

2.1 Active Galactic Nuclei

The light of normal galaxies is dominated by the thermal emission of the embedded stars [4]. Active Galaxies constitute of class of galaxies which exhibit a small region that emits radiation across the broad electromagnetic spectrum that "out-shines" the rest of the much larger galaxy.

It is found to be possible that most galaxies have nuclei that are active in such a way that in addition to the thermonuclear sources inside the constituent stars, there exists a energy source [4]. The extreme luminosity from this central nucleus of such "active galaxies" are believed to be powered by supermassive black holes (SMBHs) hosted at the very core of the system. This SMBH accretes matter from its surrounding dense region and a disk, called the accretion disk, is formed by the in-spiralling matter. This disk heats up due to frictional forces and moreover a cold dust can also be found that surrounds the central region and the accretion disk. In some AGN jets of beams of energetic particles can be ejected outward in opposite directions away from the accretion disks. And AGN, for which these jets are aligned either directly pointing to us (or at least at small viewing angles to our line of sight), the are called "blazars".

Our knowledge of AGN spectra was enhanced by the data obtained by the Infrared Astronomical Satellite (IRAS) in the far-infra red and by the Einstein, Highly Eccentric Orbit Satellite-1 (HEOA 1), European X-ray Observatory Satellite (EXOSAT) and other satellites in the X-ray domain [3].

AGN have been discovered by the optical identification of radio or X-ray sources and by a variety of studies that included only optical observations [4]. Some of the most interesting results on these sources have come through observations where several telescopes operating at different wavelengths simultaneously monitor the activity of a blazar [3]. Before AGN has been established as MeV – GeV sources by EGRET, no credible Very High Energy (VHE) detections were reported because the ground-based techniques available at the time were relatively insensitive compared to the currently available, sensitive Imaging Atmospheric Cherenkov Telescopes (IACT). Galaxies are at different distances from the Earth, but AGN characteristics may be studied best in nearby galaxies, where much detail may be seen that is unobservable in more distant objects. AGN count among the brightest objects in the Universe (with typical luminosities of $2 \times 10^{10} L_{\odot}$) and their emission can vary on a time scale of days, which leads to a size estimate for the central region smaller than 3×10^{15} cm (1 light day) [4] using the concept of light travel time. AGNs are further classified, based on their radio emission into radio-loud and radio-quiet quasars.

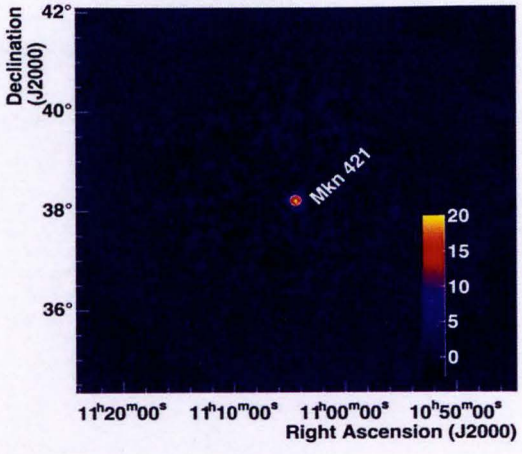

Figure 2.1 The sky map of Markarian 421 observed by H.E.S.S. after the H.E.S.S. phase I camera upgrade in 2017 [21]. The colour bar indicates the statistical significance of the detection at the various sky positions. A large significance of γ-ray detection can be seen at the position of Mrk 421, near the centre of the image.

2.2 Gamma-ray blazars

Although AGN come in a variety of classes, it is almost exclusively the blazar sub-classification of Flat Spectrum Radio Quasar (FSRQ) and BL Lacs that have thus far proven to be detectable at energies above 10 MeV [6]. Blazars include optically violently variable quasars (OVV), BL Lacs, sources that are radio-loud with compact cores, and sources that exhibit superluminal motion or strong polarization [6].

The relativistic jets of blazars pointing at angles close to the line of sight, produces emission that is dominated by relativistic effects. Blazars could also be defined as a subclass of AGN with a set of characteristic properties including a strong continuum emission extending from the radio all the way to the γ-ray regimes, and exhibit rapid variability, and show high polarization in most cases [5]. These sources have been observed at all wavelengths, from radio to Very High Energy (VHE) γ rays. The emission from blazars are known to be variable at all wavelengths. If emission lines are apparent, the blazar is called Flat Spectrum Radio Quasar (FSRQ). If no emission lines are seen, the object is classified as BL Lacertae (BL Lac) [5]. The figure below shows an SED of a blazar.

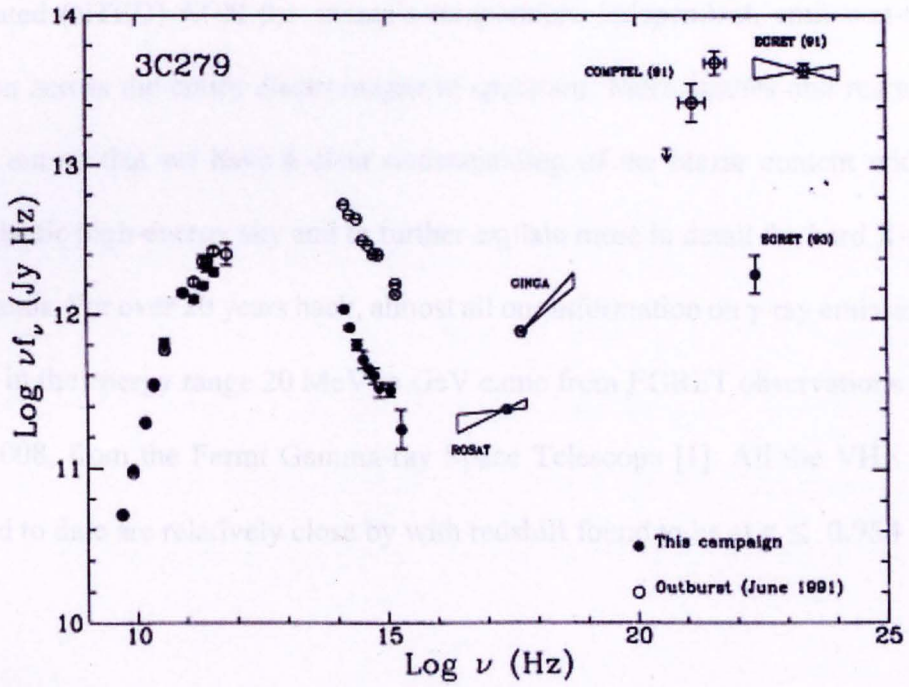

Figure 2.2 The SED of AGN, 3C 279. It shows synchrotron radiation responsible for the low energy bump and the inverse-Compton emission responsible for the second high-energy bump. This double feature is very characteristic of blazars [20].

In the SED shown in Figure 2.2, it is generally agreed that the low-frequency component of blazar SEDs might be synchrotron radiation from non-thermal, ultra-relativistic electrons and the high-frequency component might be due to Compton-scattering of lower energy photons by the same electron population. The high inferred bolometric luminosities (the total energy radiated by an object at all wavelengths), rapid variability, and apparent super luminal motions (apparently faster than light) provide compelling evidence that the non-thermal continuum emission of blazars is produced in less than the light day sized emission regions, propagating relativistically along a jet directed at a small angle with respect to our line of sight [5].

In the past years, all blazars detected at TeV energies are of the high frequency peaked BL Lac objects (HBL) type, very high energy objects and the fastest varying γ-ray sources [5]. It is now known that blazars, and in general Non-Thermal Emission

Dominated (NTED)-AGN the source's temperature independent, emit non-thermal radiation across the entire electromagnetic spectrum. More studies and research are carried out so that we have a clear understanding of the blazar content within the extragalactic high-energy sky and to further explain more in detail the hard X-ray and γ-ray bands. For over 20 years back, almost all our information on γ-ray emission from blazars in the energy range 20 MeV to GeV came from EGRET observations [6] and since 2008, from the Fermi Gamma-ray Space Telescope [1]. All the VHE blazars detected to date are relatively close by with redshift found to be at $z \leq 0.954$ [6].

2.3 Markarian 421

Mrk 421 is a blazar located in the constellation Ursa Major. The object is an active galaxy and is a strong source of gamma rays. Unlike ordinary stars that may shine in a narrow band of the electromagnetic spectrum, Mrk 421 can be seen across the entire spectrum of wavelengths, from radio to γ rays. It is about 397 million light-years to 434 million light-years from the Earth [7]. Mrk 421 is one of the closest blazars to Earth, making it one of the brightest quasars in the night sky. It is suspected to have a SMBH at its centre due to its active nature. Mrk 421 is one out of more than 1500 Markarian galaxies identified and listed during the sixties and seventies by the Armenian astrophysicist Benjamin Markarian [7]. The Markarians have only one property in common, an excessive amount of ultraviolet emission compared with other galaxies.

Unlike a quasar, BL Lac objects have no absorption lines. Their light output is highly variable over a few weeks to months and they produce high intensity emission from radio to γ-ray wavelengths. The lack of absorption lines indicates that the source of the

light is not stars; the emission indicates the presence of very hot plasma. The variability indicates that the region of bright gas is small, very much smaller than the galaxy, yet it emits as much light as the billions of stars in the galaxy.

Like the distant quasars, it appears that the root cause of the rotation at the centre of the galaxy is a SMBH. The black hole in Mrk 421 equals to a million solar mass [7]. In general, if any material, such as interstellar gas cloud, happens to pass close enough to the black hole it will form a flat disk as it orbits due to high pressure. Then, the friction of adjacent particles moving at different speeds will cause the gas to slowly spiral ever closer.

As a result of the friction, the plasma heats up to very high temperatures, which makes it emit light at different wavelengths. The emission result is two high speed jets of very hot gas going in opposite directions. In the case of Mrk 421, one of the jets appears to point right at us which we then observe. There is evidence that in the early days of the Universe galaxy collisions were much more frequent and therefore, there was more gas to fuel the quasars [8]. But galaxy collisions still occur, and Mrk 421 has a close interacting companion. The interaction with this smaller galaxy seems to have sent fresh gas into the heart of Markarian 421, fuelling the black hole that lurks there [8].

2.4 The flaring history of Markarian 421

For a historical look at Mrk 421's behaviour, the data from 22 publications were compiled by F.K. Liu [9] to assemble a long-term light curve dating back to 1900. In their study, the B band (the approximation of the raw photographic magnitude) was used since more data was available in that band than any other. The team found that in the past decade brightness variations ranged from 11.6 to 16 magnitude. Analysis of

the light curve revealed that Mrk 421 undergoes non-periodic, rapid variations on time scales of hours to days.

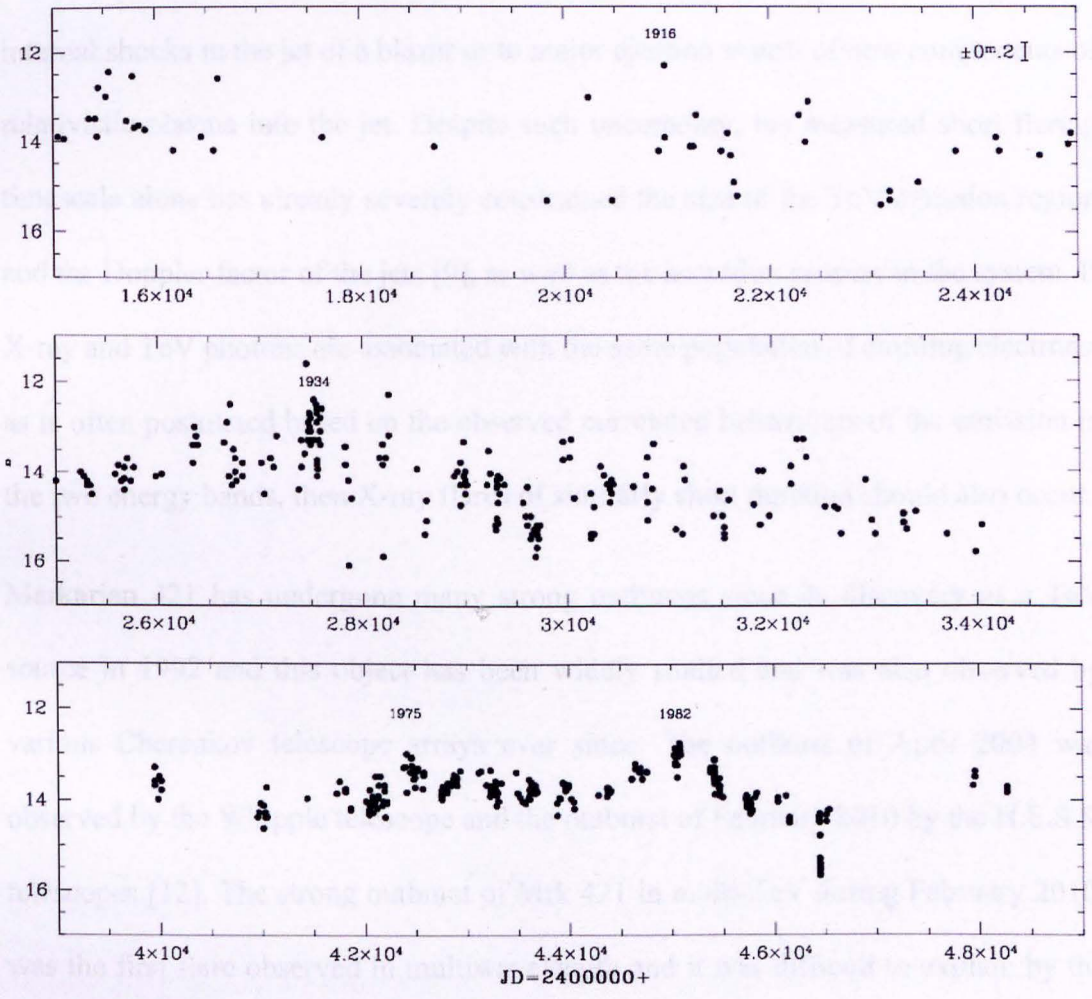

Figure 2.3 The long-term light curve of Mark 421 [9].

Additionally, they found periodic behaviour occurring at 23.1 ±1.1 years, with another possible period of 15.3 ± 0.7 years. Based on these observations, Mrk 421 has been seen to vary between 12th and 14th magnitude.

Mrk 421 is one of the X-ray sources that has been frequently observed with Rossi X-ray Timing Explorer (RXTE) over the past decades [10]. Blazars are known for their flaring activities and X-ray flares with duration of longer than a day have been observed from Mrk 421 [9]. Remarkably, a strong flare was detected from the source

at TeV energies that lasted only for about an hour [9,11]. The TeV flare shows significant sub-structures that were of even shorter durations. The origin of X-ray or TeV flares is not completely understood. The flares are often thought to be related to internal shocks in the jet of a blazar or to major ejection events of new components of relativistic plasma into the jet. Despite such uncertainty, the measured short flaring timescale alone has already severely constrained the size of the TeV emission region and the Doppler factor of the jets [9], as well as the accretion process in the system. If X-ray and TeV photons are associated with the same population of emitting electrons, as is often postulated based on the observed correlated behaviours of the emission in the two energy bands, then X-ray flares of similarly short duration should also occur.

Markarian 421 has undergone many strong outbursts since its discovery as a TeV source in 1992 and this object has been widely studied and was also observed by various Cherenkov telescope arrays ever since. The outburst of April 2004 was observed by the Whipple telescope and the outburst of February 2010 by the H.E.S.S. telescopes [12]. The strong outburst of Mrk 421 in multi-TeV during February 2010, was the first flare observed in multiwavelength and it was difficult to explain by the one-zone leptonic model [13]. The Whipple telescopes observed the flare in the energy range 0.25 TeV (6.0×10^{25}Hz) $\leq E_\gamma \leq$ 16.85 TeV (4.1×10^{27}Hz). It can be seen from Figure 2.4 below that the multi-zone fit is not so good as other fits for $E_\gamma \leq$ 15 TeV. However, for higher energies it has the same behaviour as Extragalactic Background Light model of Dominguez (EBL-D) and Extragalactic Background Light model (EBL-I) with the exponential cut-off scenario. A good fit is obtained for the spectral index $\alpha = 2.7$ and the cut-off at energy $E_c = 6.2$ TeV.

In Figure 2.4 below, the TeV SED of the flare of 2010 is plotted along with the EBL-D and EBL-I fits and their corresponding intrinsic fluxes. A minor difference can be observed between EBL-D and EBL-I predictions for 0.6 TeV $\leq E_\gamma \leq$ 20 TeV. The intrinsic flux is a power law with $F_{\gamma,in} \propto E_\gamma^{-0.7}$.

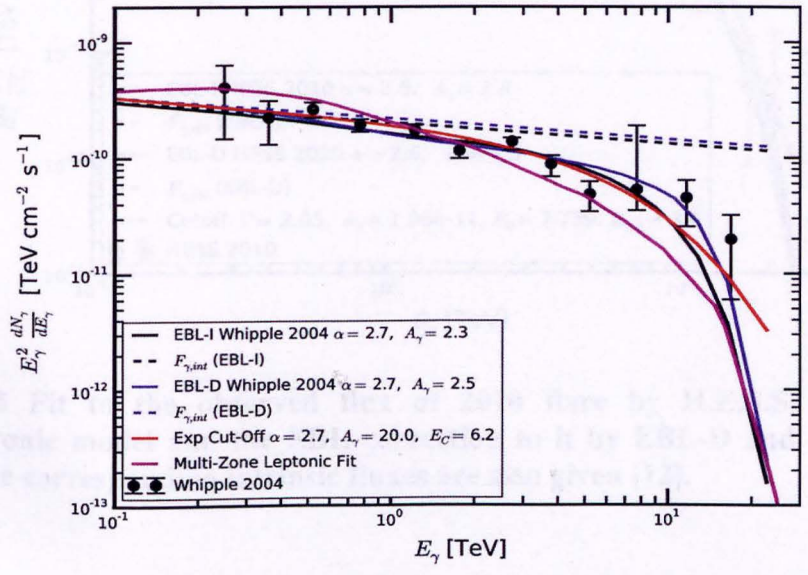

Figure 2.4 discusses to the observed flux of April 2004 flare with the photohadronic model using two different EBL models are shown. It is also compared with the power law with exponential cut-off without EBL correction fit and with the multi-zone leptonic fit. The multi-zone leptonic model accounts for the attenuation of the very high-energy gamma-rays by the diffuse infrared background. The intrinsic fluxes for the two EBL models are also shown [12].

To constrain the EBL effect on the VHE gamma-rays from Mrk 421 and to see whether the energy cut-off scenario is necessary or not, observation of VHE flux above ~ 30 TeV is a good test. A strong outburst in multi-TeV γ rays from Mrk 421 was observed by very energetic radiation imaging telescope array system (VERITAS) telescopes on 16th of February 2010 and follow up observations were carried out by H.E.S.S. telescopes from 17th to 20th of February for a total of 6.5h. These data were taken in 11 runs with each run ~28 minutes duration. The H.E.S.S. telescopes observed this

flare in the energy range 1.67 TeV (4.0×10^{26} Hz) $\leq E_\gamma \leq$ 20.95 TeV (5.0×10^{27}Hz) [12].

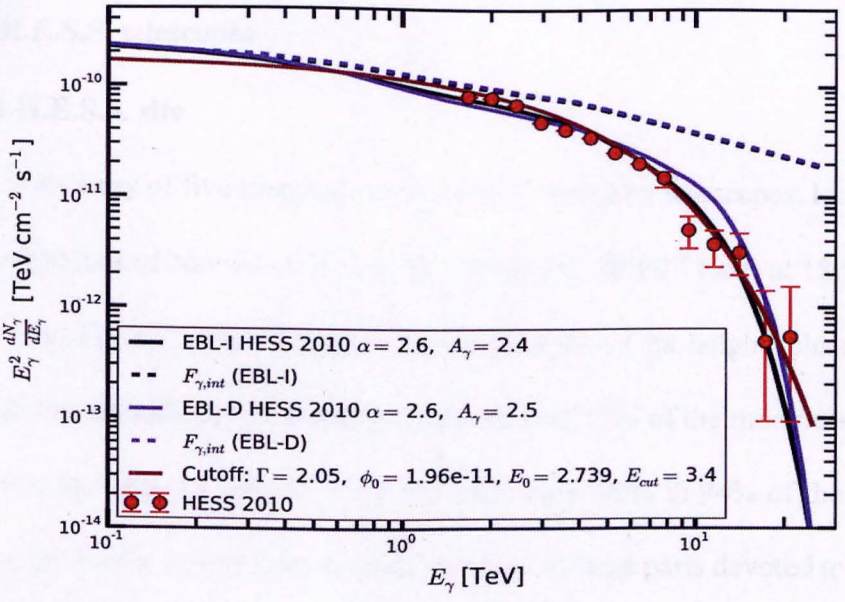

Figure 2.5 Fit to the observed flux of 2010 flare by H.E.S.S. using the photohadronic model and the EBL correction to it by EBL-D and EBL-I are shown. The corresponding intrinsic fluxes are also given [12].

Comparing the intrinsic flux $F_{\gamma,in}$ of the 2004 and 2010 multi-TeV flaring shows that the different spectral shapes of the observed events are solely due to the diversity distribution (particularly in the Synchrotron Self-Compton (SSC) tail region) even though we have the same acceleration mechanism ($\alpha \simeq 2.6$) of protons in the blazar jet.

Chapter 3

Instruments and methods

3.1 The H.E.S.S. telescopes

3.1.1 H.E.S.S. site

H.E.S.S. is an array of five imaging atmospheric Cherenkov telescopes, located in the Khomas highlands of Namibia ($23^{\circ}\ 16'18''$South, $16^{\circ}\ 30'00''$ East) at 1800 m above sea level (see Fig.3.1). This site was chosen because of its height, clear cloudless nights, and low humidity [13]. It has been shown that 57% of the moonless dark time is cloud-free and that the relative humidity was below 90% in 94% of the nights. Its location in the Southern hemisphere made H.E.S.S. in large parts devoted to the search for VHE gamma rays from galactic sources. In autumn to winter in Namibia, the galactic centre is at optimal position for observations. The H.E.S.S. experiment initially only consisted of four telescopes (CT1-4) which were built in 2002 – 2003 (H.E.S.S. phase I). A large fifth telescope (CT5) with a diameter of 28 m was built in the middle of the array (H.E.S.S. phase II) and commissioned in 2012.

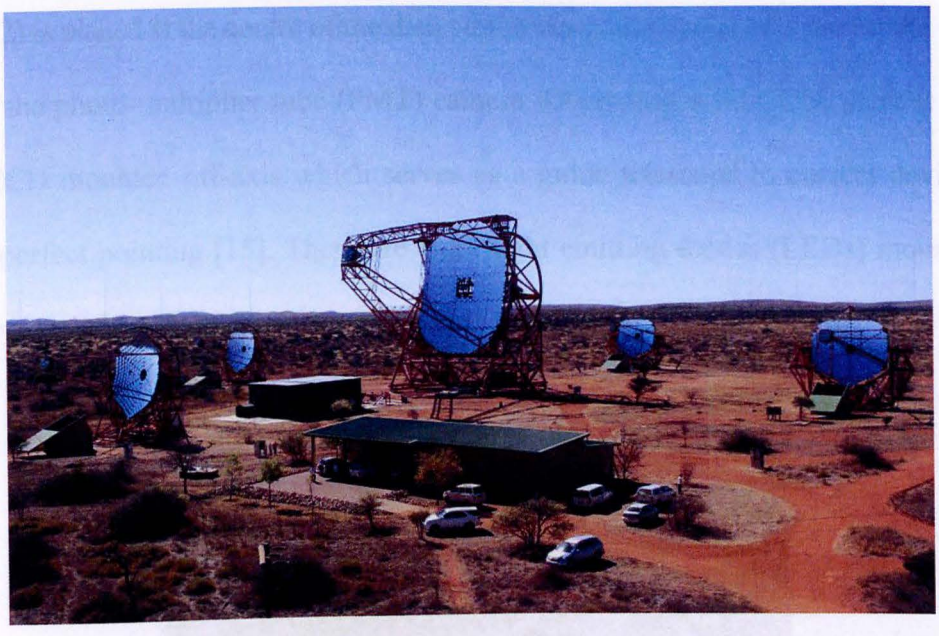

Figure 3.1 A picture of the H.E.S.S. site. The smaller telescopes CT1-4 (constituting H.E.S.S. Phase I) are located on a square of 120 m side length, while CT5, the large telescope, was introduced as H.E.S.S. Phase II in the centre of the square in 2012 the building in the foreground is also home to the Control Room from which the telescopes are controlled during nightly observations [13].

3.1.2 The layout and mirror systems

Phase I of H.E.S.S. had four telescopes, each with a 12 m diameter reflector. These telescopes are arranged in a square of a length of 120 m. The Cherenkov light pool has a diameter of 250 m [13]. This distance was optimised for maximum sensitivity at the planned energy threshold of 100 GeV. For phase II of H.E.S.S., a bigger telescope with a 28 m dish is placed in the centre of the square. It saw its first light in 2012.

For the H.E.S.S. I telescope, the dishes are made up of 382 round mirrors, each of which has a diameter of 60 cm, amounting to a total area of 108 m^2. The mirror has a $\frac{d}{f} = 0.8$ and a focal length of 15 m [14]. For a wavelength of 300 to 600 nm, the reflectivity of the mirrors is $> 80\%$ [14]. For the H.E.S.S. II mirror, the focal length is 36 m, and it is made up of 875 hexagonal facets of 90 cm diameter, each [14]. The total mirror area is 614 m^2. A charge coupled device (CCD) camera (Lid CCD, see

Fig 3.2) is placed at the centre of the dish which views the image of a star on the closed lid of the photo-multiplier tube (PMT) camera. Other than a lid CCD, there is also a sky CCD mounted off-axis which serves as a guide telescope to correct deviations from perfect pointing [15]. There are eight light emitting diodes (LEDs) mounted at the corners of the PMT.

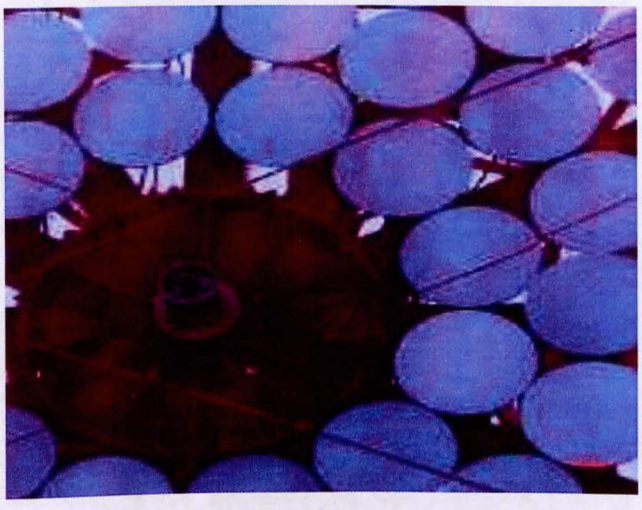

Figure 3.2 A picture of the lid CCD placed at the centre of each telescope [15].

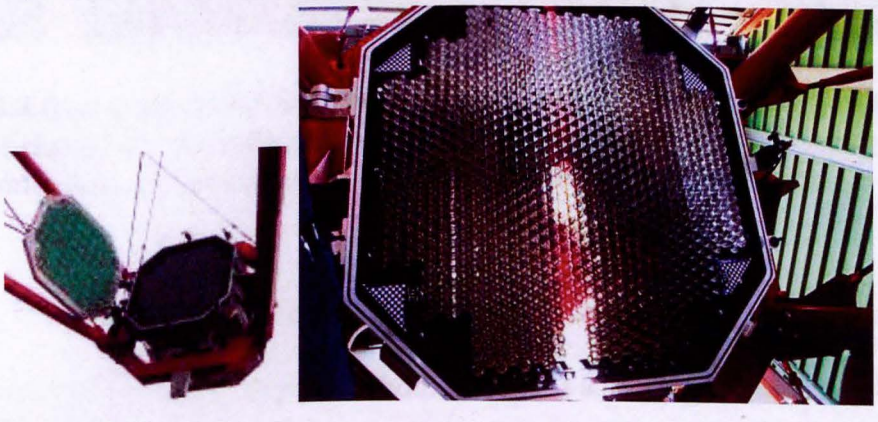

Figure 3.3 Left: The camera of a H.E.S.S. I telescope [15]. Right: A close-up view of the H.E.S.S. II camera showing the photomultipliers and Winston cones [13].

3.1.3 The H.E.S.S. Upgraded Cameras

Each telescope has a camera installed at the focal plane of the mirror. The H.E.S.S. I cameras have a hexagonal array of 960 photomultipliers (PMTs), each of which subtends an angle of 0.16°, resulting in a total field of view of 5° [24].

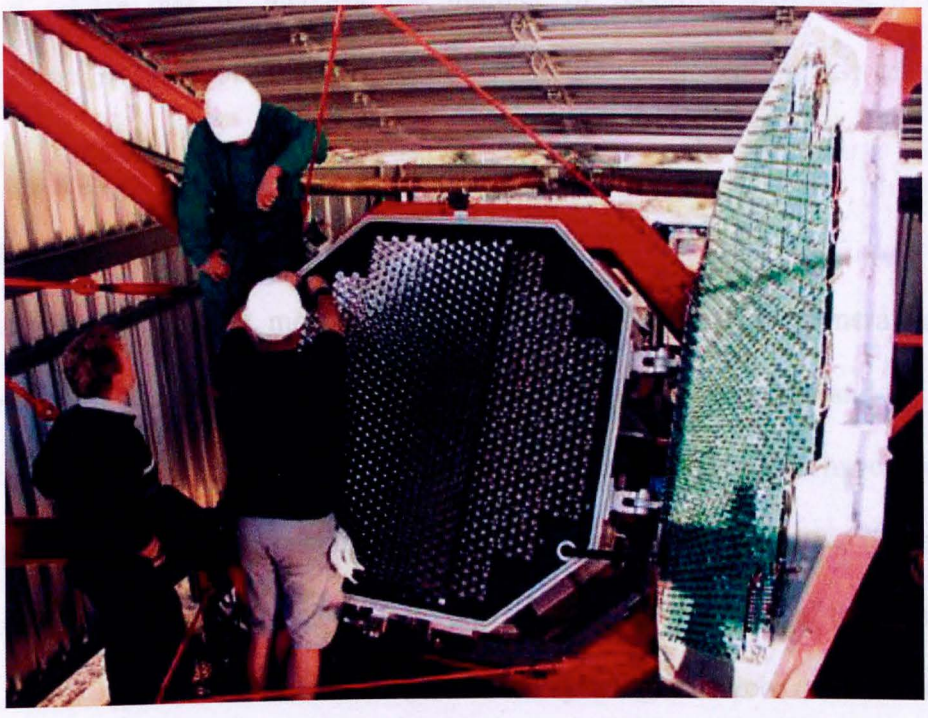

Figure 3.4 One of the H.E.S.S. I cameras in its shelter. It has 960 photomultiplier pixels of size 0.16°, resulting in a 5° field of view. The electronics with 1 GHz analog sampling rate are entirely contained in the camera body [24].

The H.E.S.S. II camera has 2048 PMTs, each has a size of 0.067° with a total field of view (FOV) is 3.2°. The front parts of both H.E.S.S. I and H.E.S.S. II, contain drawers were each of them has 16 PMTs [24]. The drawers contain the trigger and readout electronics, high voltage (HV) supply, control, and monitoring electronics [16]. A picture of HESS-I cameras is shown in Figure 3.3 above.

The larger mirror of the new telescope lowered the array energy threshold from ~100 GeV to ~30 GeV and increased the array trigger rate from 200-300 Hz [16] to more than 1.5 kHz [15]. The dead time of the old H.E.S.S. phase I camera was

$\sim 450\ \mu s$, much bigger than the dead time of the modern CT5 ($\sim 15\ \mu s$) and is not suitable for such high trigger rates. Therefore, significant fraction of the triggered events is recorded only by CT5, limiting the performance of the array [15]. Therefore, one of the main reasons or goals of the H.E.S.S. phase I upgrade is to reduce the dead time of CT1-4 and to increase the number of recorded stereoscopic events. Furthermore, because of the aging of the electronic components of the telescopes, hence, the upgrade.

3.1.4 Status of the Upgrade

As a result of the upgrade, most of the electronic components of the camera were replaced. Only photomultiplier tubes, their bases, single photoelectron and flat fielding units for calibration are the same. The upgraded cameras also have a new concept for the ventilation system [24]. Which increases air pressure and prevents dust accumulating inside the camera. Figure 3.4 (top) shows a copy of the camera body, which was used for tests of the ventilation systems, backdoor mechanics, pneumatics, centre camera trigger, etc [24].

More than 270 drawers were tested at DESY (in Zeuthen) as in figure 3.5 below with several test setups. Different characteristics were tested here: low gain (LG) and high gain (HG) linearity, crosstalk, pedestal noise, trigger path, etc [25]. The first camera (CT1) was upgraded in summer 2015 and since March 2016 has been included in regular observations. The upgrade of the other three (CT2 – 4) cameras started in September 2016 and finished in October 2016.

H.E.S.S. phase I upgrade allows to keep H.E.S.S. operating in a stable regime and improves the sensitivity of the lowest and highest energies. Moreover, the current

upgrade of the H.E.S.S. telescopes is a great opportunity to test new electronics, software and algorithms for the future ground-based experiments [25].

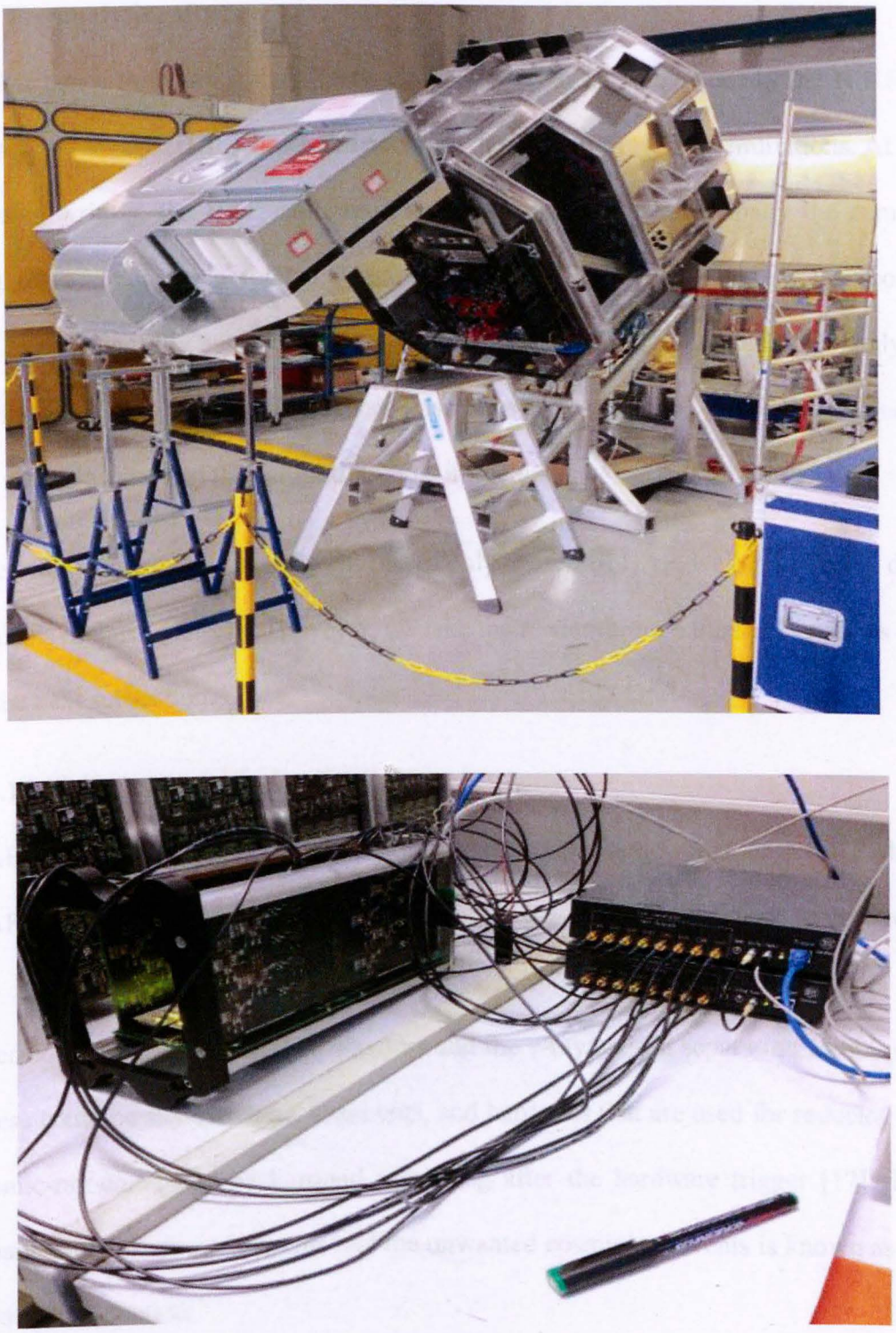

Figure 3.5 Testing setups at DESY (Zeuthen) – CopyCam (top) and test bench with pulse generators (bottom) [15].

3.2 The analysis software

In this thesis there are two H.E.S.S. data analysis software evaluated. The H.E.S.S. Analysis Package (HAP) which did not work due to data calibration limitations. At the time of writing, the HAP calibration software that was to accompany the camera upgrade was not yet completed, hence data taken with the upgraded telescope could not be meaningfully analysed at the time. As an alternative, the second data analysis chain in H.E.S.S. is the Paris Analysis (also known as Model++) which has produced the results as that had the calibration tools implemented.

Therefore, although we initially envisaged only the use of HAP, we report finally data analysis of Paris Analysis. However, we take the reader through the HAP analysis toll in the next subsection.

3.2.1 The H.E.S.S. Analysis Package

HAP is one of the supported analysis and reconstruction frameworks for H.E.S.S. data. HAP has been released in two flavours called HAP-HD and HAP-France representing the Heidelberg and France research groups, respectively. Different data sets are selected depending on the HAP flavours and the γ-ray/hadron separation techniques. These could be standard cuts, loose cuts, and hard cuts that are used for reducing the cosmic-ray-dominated background remaining after the hardware trigger [17]. This separation between γ-ray events and the unwanted cosmic ray events is known as the γ-hadron separation.

H.E.S.S. uses the following separation techniques:

- Standard cuts are mostly used for sources with a flux at the level of ~10% of the integral flux of the Crab Nebula and with a spectrum similar to that of the Crab Nebula, i.e., spectral index Γ~2.5. These cuts are based on Toolkit

Multivariate Data Analysis (TMVA) analysis [27] and include a 60-photoelectron cut on image intensity.

- Hard cuts are often used for weak sources exhibiting a ~1% flux of the Crab Nebula with hard spectra Γ~2.0. They are also based on TMVA analysis and include a 160-photoelectron cut on image intensity. The hard cuts increase the energy threshold because of the stricter cut on the image amplitude.
- Loose cuts are optimised for strong sources with an integral flux similar to that of the Crab Nebula and a steeper spectrum of photon index Γ~3.0. Loose cuts are also based on TMVA analysis and allow a 40-photoelectron cut on image intensity. These cuts require a low energy threshold and are the loosest in the sense of rejecting the smallest number of events.

3.2.2 Installing HAP

HAP is installed in the following two steps.

Step 1. Compiling HAP

HAP uses the *SCons* Build System for compilation and linking. To build HAP,

```
source ./thishess.sh
scons --checkout-missing=hap-18 HAP
```

The first command sets the required environment variables whiles the second command initiates the building process. During building, *SCons* makes sure that H.E.S.S. software modules needed for the build are retrieved from the CVS automatically.

Step 2. Quick check

To test if HAP was built properly,

```
$HESSROOT/hddst/bin/hap
```

Then if correctly built, it prompts,

```
hap> ------------------------------------------------
hap> This is HAP version hap-18-pl00.
hap> ------------------------------------------------

****** CREATE NEW HESSARRAY WITH NEW SYSTEMS *****
SashAstro::Initializer> SashAstro::Initializer::SetSystems
MonoDirectionMaker> Using hillas object: Hillas0510 to make shower
ChainShower
MonoEnergyMaker> Using hillas object: Hillas0510 to make shower
ChainShower
MonoPIDMaker> Using hillas object: Hillas0510 to make shower
ChainShower
MonoEnergyMaker> Deleting EnergyMaker
NAME
    hap - The HESS Analysis Program. This program processes DST
(Data Set) or
    MiniDST files and outputs the final analysis (maps and
statistics).

CONFIGURATION OPTIONS:

    Global options:
    --AddBrokenPixelFile
        Add the corresponding Broken pixel file to the Observation
        run!
        Default is: false

    --AddCameraFile
        Add the corresponding Camera file to the Observation run!
        Default is: false


[...]
```

which shows the HAP version number and a lot of command line arguments to configure the analysis.

3.2.3 Cut Configuration Files

For proper analysis, a set of predefined analysis cuts were chosen. These cuts are defined in a series of HAP configuration files and lookup tables.

HAP expects the configurations to reside in a special location given by the `$HESSCONFIG` environment variable, meaning that the configurations must have been installed on the machine and the `$HESSCONFIG` variable points to the installation path of the configurations. As an example, on the MPIK Heidelberg cluster:

```
> echo $HESSCONFIG
/lfs/l2/hess/analysis/version36
```

3.2.4 Using HAP-a step-by -step analysis

In this section a H.E.S.S. I HAP analysis on Mrk 421 is presented, which produces a sky map of the region using the ring background technique, with no spectral analysis. The ring-background method is typically used to visualise the excess of γ rays attributed to a source of two-dimension sky map. The task of a background model is to provide the quantities α and N_{off}. The parameter α reflects the relative acceptance A of the test region and the control region [18], and can be defined as:

$$\alpha = \frac{\iint A_{on}\, d\emptyset\, d\theta}{\iint A_{off}\, d\emptyset\, d\theta}.$$

This method also uses a ring around a trial source position (in celestial coordinates) to provide the estimate of the background. However, the consistency of the acceptance within the ring cannot be assumed to be true because the ring covers areas with different offsets from the observation position.

3.2.5 Obtaining a list of runs

The Heidelberg run selection tool is used to generate a list of runs from the Markarian 421 region:

```
> $HESSROOT/summary/scripts/findruns.pl --name "Mrk 421" --selection spectral 1.5
```

This command searches the database for observation runs taken no more than 1.5 degree away from the position of the Mrk 421. It only selects runs which have been flagged as suited for spectral analysis by the data quality selection. However, in the case of this project the Mrk 421 January 2017 flare runs were known and there was no need on searching for the runs with the '`findruns`' tool.

127739

127738

127737

127736

127725

127724

127723

3.2.6 Making a configuration file

The simplest way to make a configuration file is to have HAP make a sample one, which can be edited. For sample config file, the syntax is

```
> hap --sampleconfig myconfig.conf
```

Which will produce a file called `myconfig.conf` with all available options. Default options are marked as such in the file. Below is a HAP configuration file for Mrk 421.

```
[OPTIONS]
        verbose = true
        mc = false
        outdir = /home/extern/tnanghonga/source-mrk421
        outfile = runlist_hap_3c279_02.lis
        runlist = mrk421.lis
        config = loose_ImPACT_hybrid

[Background]
        Method = ReflectedBg # use a ring background
        FOV = 4.0       # size of resulting maps
        TestPosRA = 166.119
        TestPosDec = 38.207

        AcceptanceFromData=true
        MaximumEventOffset = 1.6
        ExtraMethods = RingBg
        SafeEnergyRangeOnly = true

        AcceptanceCurveSmoothingDegree = 9
        AcceptanceCurveSmoothingBins = 14000

        DisableSafeEnergyTrigger = false
        AllowedEnergyBias = 0.10 #new try it was 0.2 in the
previous attempt
        #ExclusionRegionsFile =
/d1/hfm/cromoli/HESS/pks2022/ExcludedRegions.dat


[Analysis]
        MiniDST = false
        UseNewHDMuon = true
        UseEffAreaSafeThresh=true

[Spectrum]
        Method = Standard
        AllowedEnergyBias = 0.10
        EnergyMaxArea = 10000
[RingBgMaker]
        InnerRingRadius = 0.4
        AdaptiveMaxRadius = 1.7
        RingThickness = 0.2
        AdaptiveRing = true

[Lightcurve]
    Generate = true                    # Turn on the making of
Lightcurve
    LightcurveName = Lightcurve        # Name of the Lightcurve
Object
```

Chapter 4

Results

In what follows we show the step-by-step command execution of the HAP analysis that runs the analysis and extracts the results.

4.1 Running HAP

HAP is called with the two config files as command line options.

```
> $HESSROOT/hddst/bin/hap --include Mrk421source.conf
```

The command above uses the variables as declared and initiated inside the file named "`Mrk421source.conf`" and feed that to the "hap" tool to run the analysis. Amongst others this configuration file provides HAP with the name, location, and type of cut analysis that are desired.

4.2 Looking at the output

All output from HAP is placed in a subdirectory called `runlist.hap/` (where `runlist` is the name the runlist in the configuration file). The following output are found in that directory:

- **ROOT data:** the data and plot output is saved in a file called `runlist-config.root` (here Mrk421_1.5_loose.root)
- **Log file:** `Mrk421_1.5_hard.log.conf` contains all of the configuration options used in the analysis (including default values). Each time the analysis is run, the new configuration is appended to the end of this file. It can be used to see exactly what was run and is itself a valid configuration file which can be used to run HAP in case the original configuration is lost.

4.3 Producing output plots

For a quick look at the results

```
$HESSROOT/hddst/bin/hap-show -file Mrk421_1.5_hard.root
```

which produces the output plots. The results could not be produced because this was one of the first datasets taken with the (then) newly upgraded HESS-I cameras and at that time the new corresponding IRFs (Instrument Response Functions). The IRFs takes care of the response of the telescopes which depend on many phenomena such as the telescope orientation, background light, and weather conditions. The necessary adjustment that is enabled by these IRFs to the data, particularly in producing calibration tables and final analysis-ready DSTs (Data Sets) were not yet available when this analysis was attempted.

4.4 Paris step-by-step analysis

4.4.1 The analysis commands

Paris analysis functions on the Linux operating system the same away as for the HAP. Below are some analysis steps that were followed during Mrk 421 data analysis.

```
source setHESS_34.sh
```

this locates or sources the file in the database.

```
[tnanghonga@uhpc ~]$ gpa
```

This prompts the Paris analysis graphic user interface which contains tabs such as submit analysis, merge slices and submit merging. The analysis was done in different slices and these slices had to be merged to become one after the analysis has finished.

```
[tnanghonga@uhpc ~]$ qstat
```

This shows the number of analysis submitted and which are in queue for running.

4.4.2 Viewing at the output

The ROOT software (written in C++) is used to view the results using the next command

```
[tnanghonga@uhpc~]$root1Results_Mrk_421_ModelPlus_Combined3_St
d.root
```

This goes into the directory where the finished analysed results are store in the root.

```
root[2] results→GetEntry()
```

this allows to access to a specific file (results) and this can also be used for different files with different names.

```
root [3] new TBrowser()
```

it browses the graphic user interface of all results where the specific plots or tables of results can be found and viewed. The wanted results can be saved from this interface on a host machine which can then be copied to a local machine.

This uses the secure copy technic that is used to copy files or directories from or to host machine and local computers.

Previous studies showed that the gamma-like event distribution in the Model ++ analysis is not always symmetric around the centre of the field of view. The multiple off method, which is used to subtract the background and compute spectra, does not take into account the non-axisymmetric behaviour and therefore tends to produce

unstable results when the non-axisymmetric effects are significant. The ring background technic, which uses a 2D acceptance model, is also affected. This implies that the non-axisymmetric features are not constant, as measured in the camera field of view coordinates.

The spectrum of VHE blazars that is measured on Earth can be described with the terms given by:

$$\emptyset(E,Z) = \emptyset_{int}(E) \times \exp(-\tau(E,Z,n))$$

where $\emptyset$ is the measured flux, E is the γ-ray energy and Z is the redshift of the source. The term $\emptyset_{int}$ is the intrinsic spectrum, which is independent of cosmic evolution factors, factors contributing to the rise of complexity in nature, for local blazars. The optical depth τ for a gamma ray of energy E emitted at a redshift Z depends on the density n of target EBL (Extragalactic background light) photons. The power-law (PWL) explains the simplest energy dependence of an emitted spectrum. A linear function in log-log scale:

$$\text{PWL: } \emptyset_{PWL}(E) = \emptyset_0(\frac{E}{E_0})^{-\Gamma}$$

Which is defined with the normalization factor $\emptyset_0$ and the photon index Γ. E_0 is the reference energy which can be fixed. On the theoretical background the exponential cut off is expected which can be described by the exponential cut-off power-law model:

$$\text{EPWL: } \emptyset_{EPWL}(E) = \emptyset_0(\frac{E}{E_0})^{-\Gamma} \exp\left(-\left(\frac{E}{E_{cut}}\right)^{\epsilon}\right)$$

where E_{cut} is the cut-off energy.

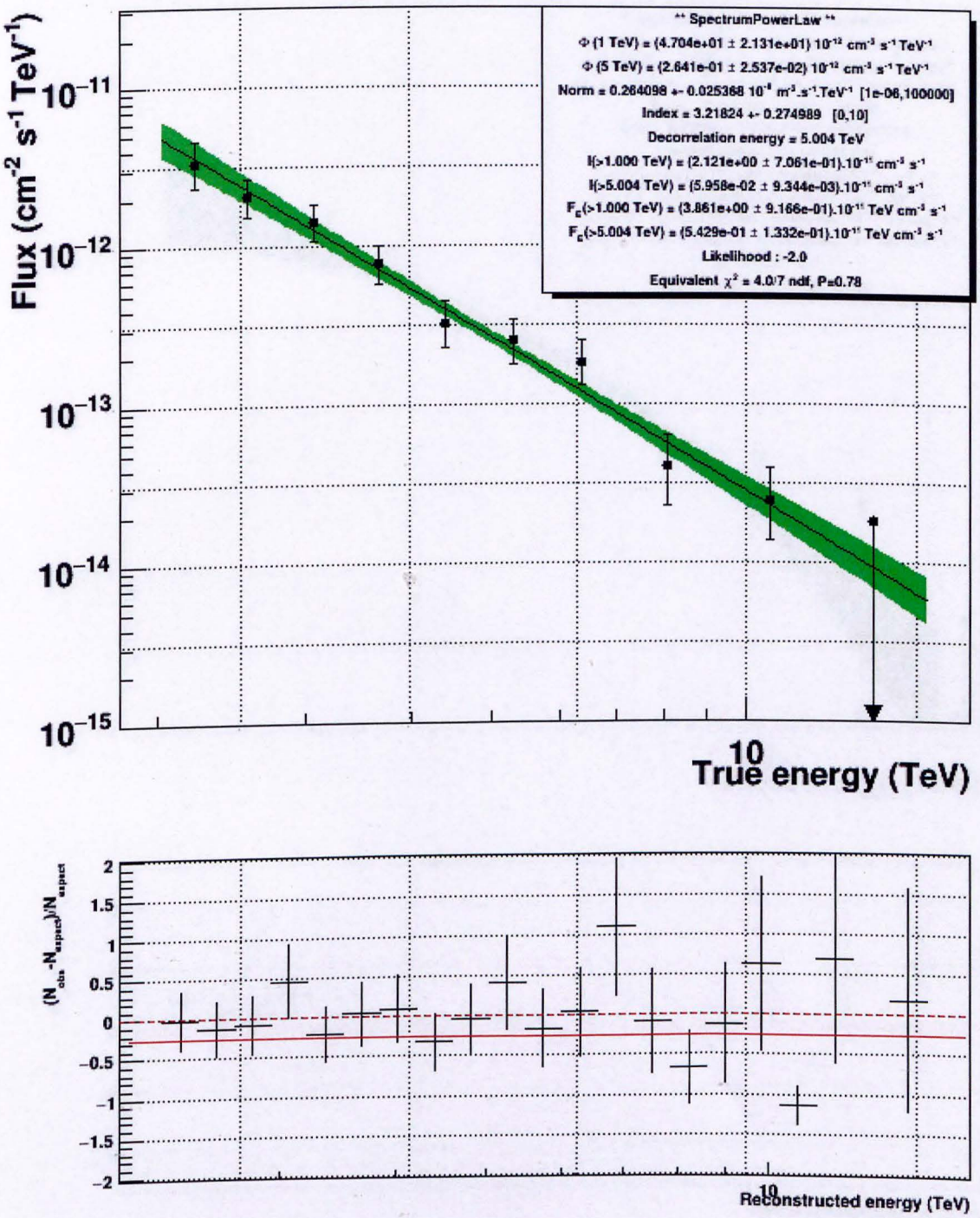

Figure 4.1 Top: Energy spectrum described by a power-law with spectral index 3.22± 0.27 decreasing in flux as the energy increases. Bottom: Residual plot.

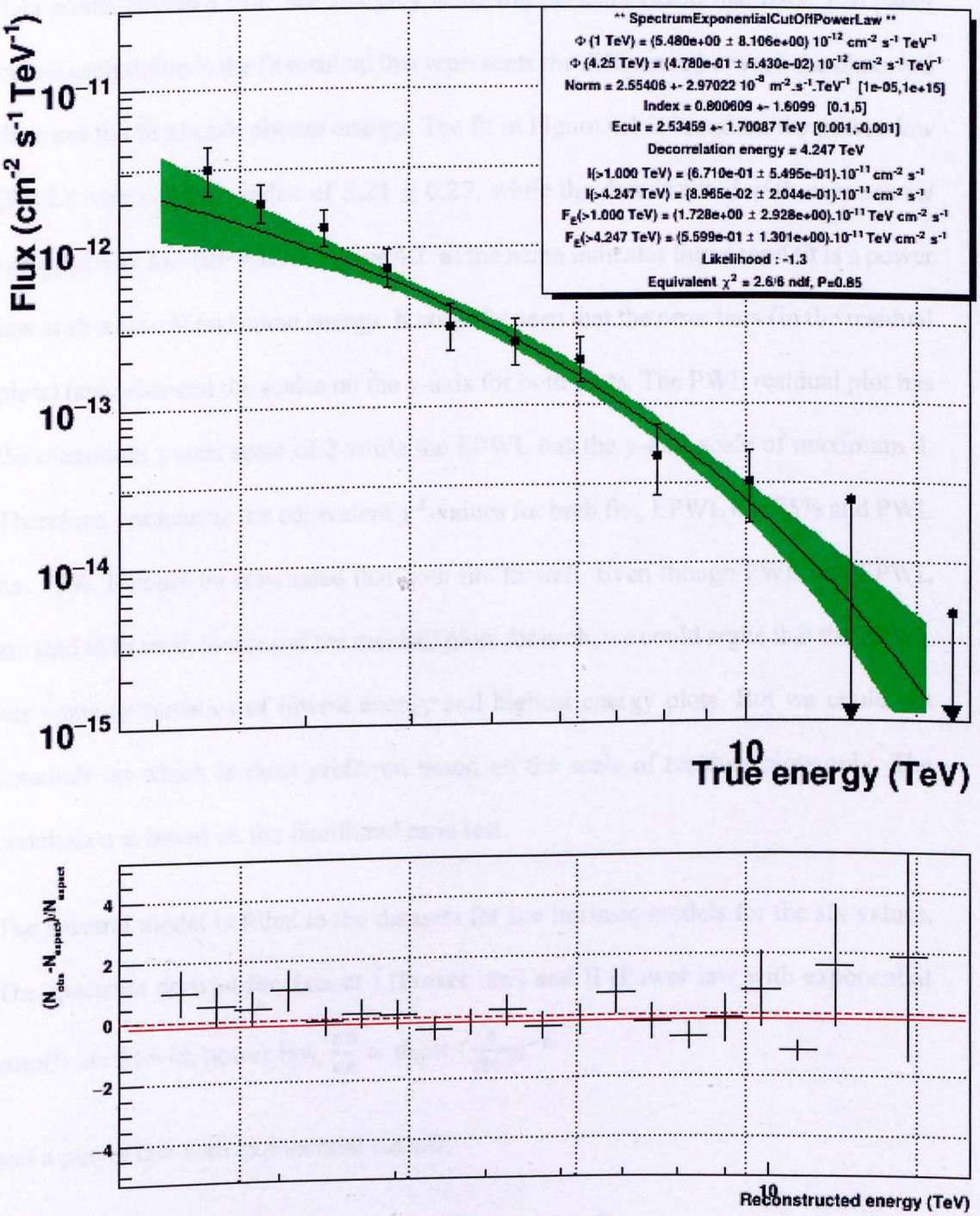

Figure 4.2 Top: Energy spectrum described by a power-law with exponential cut-off is observed to have the spectral index 0.80 ±1.61 with the exponential cut at 2.53 ±1.70 TeV energy. Bottom: Reconstructed energy.

Looking at the SEDs shown in both Figures 4.1 and 4.2, the dots represent the observed data points obtained from the analyses while the lines are fits to that data. The panel below each figure is the fit residual that represents the difference between the observed data and the fit at each photon energy. The fit in Figure 4.1 is based on the *power law* (PWL) with a photon index of 3.21 ± 0.27, while the data is fitted with *exponential cut-off power law* (EPWL) in Figure 4.2. as the name indicates the second fit is a power law with a cut-off and some energy. It could be seen that the error bars (in the residual plots) have changed the scales on the y-axis for both plots. The PWL residual plot has the maximum y-axis scale of 2 while the EPWL has the y-axis scale of maximum 4. Therefore, comparing the equivalent χ^2-values for both fits, EPWL has 85% and PWL has 75%. It could be concluded that both fits fit well. Even though PWL and EPWL are said to fit well, looking at the residual plots for each, we could argue that the EPWL has some systematics of lowest energy and highest energy plots. But we could not conclude on which is most preferred based on the scale of residual plots only. The conclusion is based on the likelihood ratio test.

The spectral model is fitted to the datasets for the intrinsic models for the six values. The spectrum derived for dataset I (Power law) and II (Power law with exponential cutoff) are fit with power law, $\frac{dN}{dE} = \Phi_0 \times (\frac{E}{1TeV})^{-\mathrm{r}}$

and a power law with exponential cut-off,

$$\frac{dN}{dE} = \Phi_0 \times (\frac{E}{1TeV})^{-\mathrm{r}} \times e^{(\frac{E}{E_{cut}})^{\beta}}$$

Where Φ_0 is the flux normalisation in $\mathrm{TeV}^{-1}\mathrm{cm}^{-2}\mathrm{s}^{-1}$, $-\mathrm{r}$ the spectral index and E_{cut} the energy cut-off. β is the strength of the cut-off which is taken to be one. Figure 4.1 shows the results of the fit of power law and figure 4.2 shows the results of the fit of

power law with exponential cut-off. For the dataset I, the results of χ^2/dof for power law with exponential cut-off is 2.66/0.85 whereas that for power law fit is 4.07/0.78. by comparison for the duo, it is found that power law with exponential cut-off makes a better fit to the data.

The index, energy cut-off and flux normalization at 1 TeV and integrated flux above 1 TeV for dataset I are found to be

$$\mathrm{r} = 3.22 \pm 0.27$$

$$\Phi_0 = (4.70 \pm 2.31) \times 10^{-12}\mathrm{cm}^{-2}\mathrm{s}^{-1}$$

$$\Phi(\geq 1\ \mathrm{TeV}) = (2.64 \pm 2.54) \times 10^{-12}\mathrm{cm}^{-2}\mathrm{s}^{-1}$$

The index, energy cut-off and flux normalisation above 1 TeV and integrated flux found for power law with exponential cut-off are:

$$\mathrm{r} = 0.80 \pm 1.61$$

$$E_{cut} = 2.53 \pm 1.70\ \mathrm{TeV}$$

$$\Phi_0 = (5.48 \pm 8.11) \times 10^{-12}\mathrm{cm}^{-2}\mathrm{s}^{-1}$$

$$\Phi(\geq 1\ \mathrm{TeV}) = (4.78 \pm 5.43) \times 10^{-12}\mathrm{cm}^{-2}\mathrm{s}^{-1}$$

The values found for both datasets are not much consistent with previously published H.E.S.S. results [26], which is $(2.1 \pm 0.04) \times 10^{-12}\mathrm{TeV}^{-1}\mathrm{cm}^{-2}\mathrm{s}^{-1}$ for index, 15.7 ± 3.41 for energy cut-off, 2.55 ± 0.06 for flux normalisation, and $(1.99 \pm 0.09) \times 10^{-12}\mathrm{cm}^{-2}\mathrm{s}^{-1}$ for flux above 1 TeV. For power law fit, no cut-off is seen in the spectrum. There is not enough high energy statistics to tell whether an energy cut-off exists.

The likelihood ratio test is used to compare the two models, SpectrumPowerLaw and SpectrumExponentialCutOffPowerLaw. It could be observed from the above Figure 4.4 and Figure 4.2 that the likelihood $L_1 = -2.0$ for PWL and $L_2 = -1.3$ for EPWL.

Calculating the likelihood scores of the two models, we take the natural logarithm of L_1 and L_2

$$\ln|L_1| = 0.693147$$

$$\ln|L_2| = 0.262364$$

The difference in the degrees of freedom between the two models is 1. Similarly, lambda can be found to be

$$\lambda = \frac{L_1}{L_2} = 1.538462.$$

From the above logarithm values the chi-square value can be calculated by

$$X^2 = 2\ln\left({}^{L_1}/_{L_2}\right) = 0.861566.$$

It is found that the probability of the more complex model (EPWL) fitting the data better than the power-law model is 27.9% and the corresponding significance level is 0.35. For the significance level p=0.05, the critical value for the likelihood ratio test is 3.84, far from the 0.86 obtained here.

Following the likelihood ration test, and from the observation that the probability of EPWL is 27.9% which is lesser, then the power-law model is preferred over the model with exponential cut-off.

4.5. The ring background method

The ring background is typically used to visualise the excess of γ rays attributed to a source of two-dimensional sky maps. In the case of the sky map, the algorithm starts from a binned map of the events registered in the observation. For each pixel, it then determines an estimate of the residual cosmic-ray background for that pixel by summing up the events in all pixels contained in a ring around the pixel with inner radius r_{min} and outer radius r_{max} .

4.5.1 Sky Maps

The γ-ray excess may also be visualised in the form of sky maps, particularly in the case of spatially extended sources. Because different quantities can be plotted; here the focus is on the common case of sky maps denoting the significance of an excess.

A potential excess of γ-ray events can then be determined by subtracting the background estimate from the map of registered events. Similarly, the significance of the excess can be computed. The γ-ray excess may also be visualised in the form of sky maps, particularly in the cases of spatially extended sources.

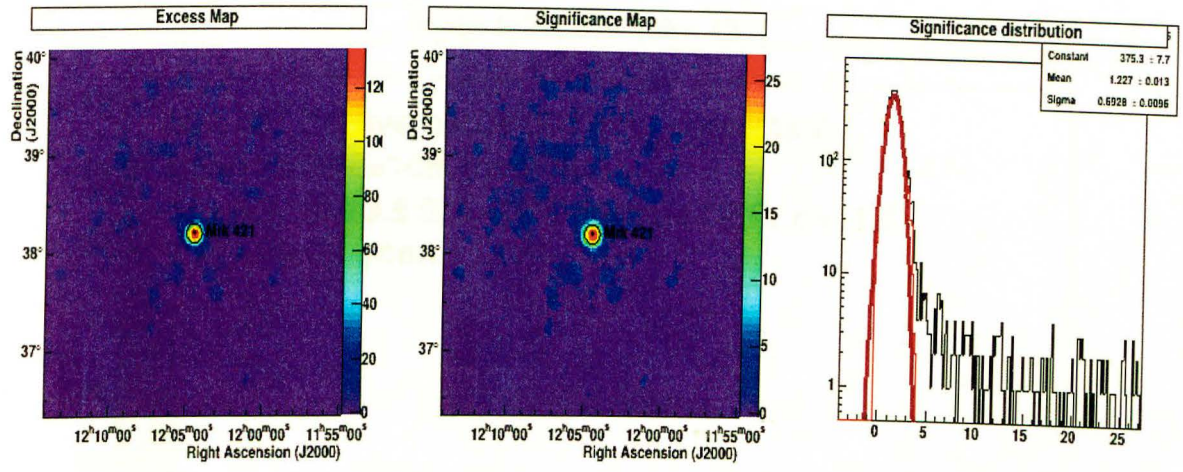

Figure 4.3 Left: Excess map showing the source position. Middle: the significance map. And right: significance distribution with the mean value 1.22±0.01.

It could be observed from the significant distribution above that, the normal distribution (in red) shows no source in the map for significance that are < 5. The many outliers towards high (positive) significances > 5 clearly indicate the presence of a source.

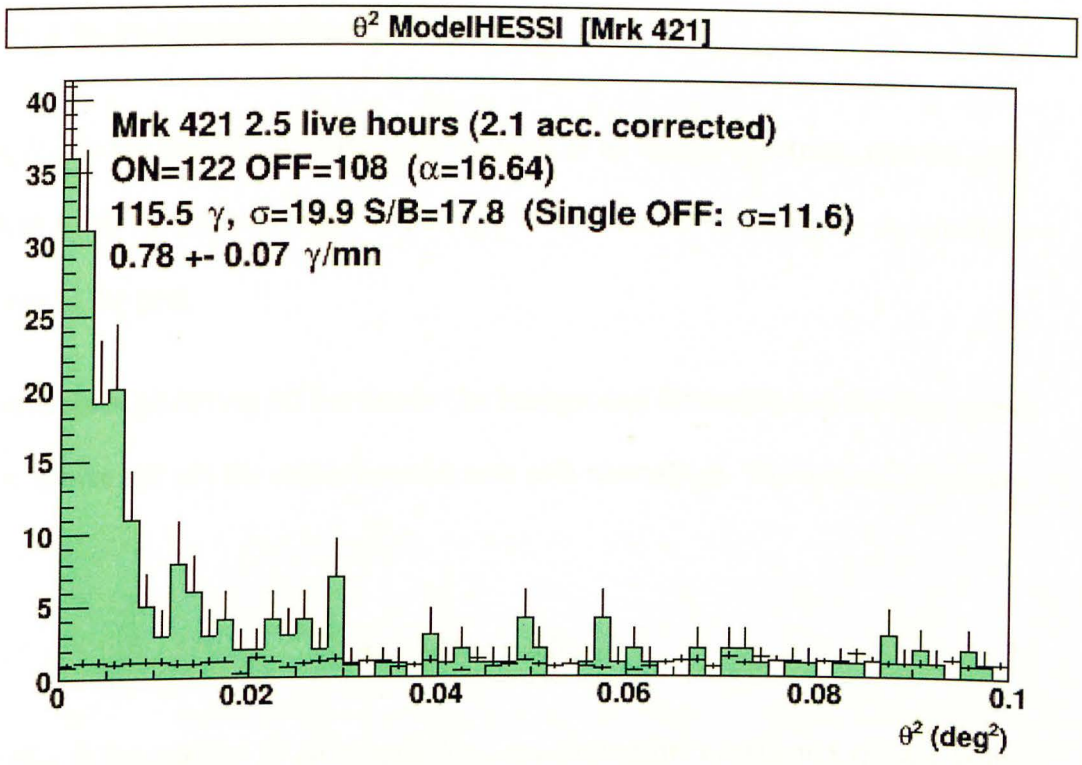

Figure 4.4 The θ^2 distribution is often used to display the excess of γ rays from the position of the source, especially for point like sources. The map is demonstrating that the instrument (H.E.S.S.) response function is processed correctly by Parish analysis.

In Figure 4.4, also called the $\boldsymbol{\theta^2}$-plot, the vertical axis represents the number of events observed for the squares of various angular distances along the horizontal axis. These angular distances θ (in units of degrees) are obtained by taking the difference between the known source direction and the reconstructed direction of the observed γ-ray event. As this $\boldsymbol{\theta^2}$-plot peaks at values close to zero of the angular distance one concludes that most events are incident from proximity of the source. To further quantify this implied source detection, one determines the excess of γ-ray events N_{excess} that comes from the source. The statistical significance σ of this excess of detection is computed as follows [18]:

$$\sigma = \frac{N_{on} - \alpha N_{off}}{\sqrt{N_{on} + \alpha^2 N_{off}}}$$

were α is the background normalization, $\alpha = \frac{n_s}{n_b}$

Here, N_{on} is the number of counts under a peak in an energy spectrum, and the peak is taken to be n_s channels wide while N_{off} is the number of counts in n_b channels adjacent to the peak.

The time spent observing off the source (for background estimates) and the time spend on the source are not the same, hence α acts as a normalizer. The excess counts are then

$$N_\sigma = N_{on} - \alpha N_{off}$$

were N_{on} is the number of on events, N_{off} number of off events and N_{excess} is the number of excess events.

This $\boldsymbol{\theta^2}$ distribution therefore often used to display the excess of γ rays from the direction of the source, especially for point-like sources. Figure 4.4 shows such a distribution for Mrk 421 data set, here obtained with Paris Analysis (or Model++ Analysis). It could be observed that with the Model++ standard cuts analysis, an excess of $N_{excess} = 115.5$ γ rays, for $N_{on} = 122$ on-source and $N_{off} = 108$ off-source events are detected at the 19.9σ significance level. It is customary in γ-ray astronomy to regard any significance greater than 5σ as a statistically significant detection of the source. And again, the plot also shows that more γ rays are detected at the lowest angle of $\boldsymbol{\theta^2}$ and the count of events decreases as the angle increases (as we go further outward from the source position).

4.6. The reflected background method

The reflected background method is usually employed to determine the flux of gamma rays from a given source, in other words, to extract its spectrum. The source is

observed under a small offset with respect to the pointing direction of the telescopes. The extraction of the spectrum then proceeds by determining the excess of γ-ray events in the on-region with respect to the off-regions and performing a forward-folding likelihood fit, utilising the instrument response functions. Both techniques, ring-background and reflected background extract the flux of γ rays from a source by determining the number of registered events in a region of interest, called on-region, and comparing this to an estimate of the residual cosmic-ray background, obtained from one or more multiple off region(s) within the field of view.

4.7. The light curve

A light curve is a graph that shows the brightness of an object over a period. In the study of objects which change their brightness over time, such as Mrk 421, the light curve is a simple but valuable tool to a scientist. Light curves can be generated for any measure of brightness which is measured over time.

In this case time is given in terms of the Modified Julian Date (MJD), is a modification of the Julian date that is routinely used by astronomers, geodesists, etc. This dating convention, designed to facilitate simplified chronological calculations, numbers all days in consecutive fashion, beginning at a date sufficiently far into the past to precede the historical period. The Julian Date (JD) was a continuous count of dates before the concept of the MJD, and is defined as the absolute count of the number of days since noon 1 January 4713 BC (the beginning of the so-called Julian Period) and the system seems to be often reported as being named after Julius Scaliger [19]. The MJD is then obtained by reducing the JD by computing

$$MJD = JD - 2400000.5$$

Taking all this into account, the reference epoch (starting point) of the MJD is November 17, 1858.

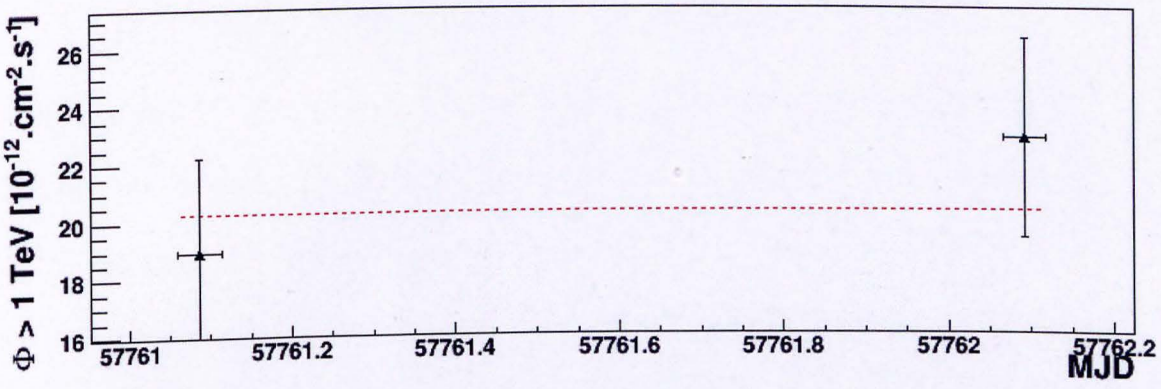

Figure 4.5 The night-by-night light curve that shows the average flux per night as a function of MJD.

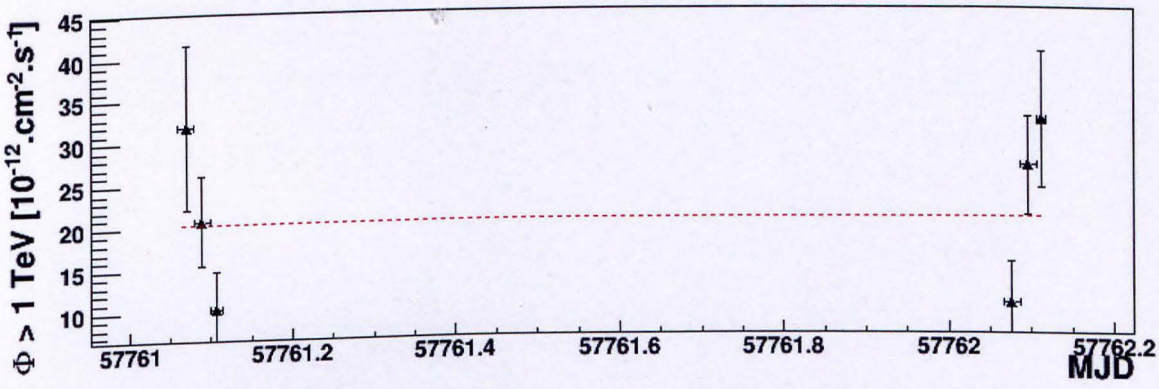

Figure 4.6 The run-by-run light curve that shows the brightness recorded at different energies for each observed run.

Figure 4.5 shows weighted average of the run-by-run fit which indicates every run per night. The average observed flux above 1 TeV is found to be 2.1×10^{-11} cm^{-2} s^{-1} TeV for both run-by-run and night-by-night. Due to the scarcity (few datasets) of data, no significant variability (any pattern of flux change as function of time) could be observed. Furthermore, it is unfortunate that not much can be learned

from the light curve due to the latter. We could see from Section 4.4 above that for a constant fit, the calculated Chi^2/dof = 2.26377 for fitting the 2 points in figure 4.5 and Chi^2/dof = 0.452754 for fitting 6 points in figure 4.6. This represents a good fit because 0.452754 is close to 1 which satisfies Chi^2/dof ~1 for a good fit.

Chapter 5

Conclusion

In classical analysis of γ-ray data from imaging Cherenkov telescopes (IACTs), such as H.E.S.S. is applied in a region of interest (RoI) encompassing the source.

In this thesis, the blazar, Mrk 421 as a source of γ rays is demonstrated by the experimental data recorded by the H.E.S.S. system of Cherenkov telescopes in January 2017. The analysis was done with two different analysis software packages. The first analysis was with HAP, which could not produce all the results due to data calibration limitations. That is, this was one or the first datasets taken with the newly upgraded HESS-I cameras. The necessary adjustments to the software, particularly in producing calibration tables and data sets (DSTs) were not yet available when this analysis was attempted. The second analysis is Paris Analysis which had worked well and has produced the expected results.

In chapter 4, the procedure for constructing the model template for the excess map, significance map and the ring-background map is outlined. Finally, in chapter 4, the H.E.S.S. data analysis results are discussed. As it could be observed from Figure 4.4 that, with the Model++ (Paris Analysis) standard cuts analysis, an excess of 115.5 /gamma rays, for $N_{on} = 122$ on-source and $N_{off} = 108$ off-source events are detected at the 19.9σ significance level. It is therefore noted that the data set used for analysis in this thesis has various limitations: it comprises of only few observations (7 runs) taken in January 2017 because of the fluctuations of the weather, on relatively strong γ-ray source. Therefore, Following the likelihood ration test, and from the observation that the probability of EPWL is 27.9% which is lesser, then the power-law model is preferred over the model with exponential cut-off.

. However, I am confident that the analysis concept can also be applied to larger data sets in the future.

References

[1] Morselli, A., 2011, "*Testing Astroparticle Physics with the Fermi Large Area Telescope*," Nuclear Physics B -Proceedings supplements, **212-213**, 343.

[2] Andreas, T. and HAWC Collaboration. 2012, Journal of Physics: Conference Series **375**, 052026.

[3] Blandford, R.D., Netzer, H., Woltjer, L. 1990, "*Active Galactic Nuclei*," Springer Science+Business Media, LLC., **1**

[4] Kellermann, et al. 1994, "*The radio structure of radio quiet quasars in the Palomar Bright Quasar Survey*," The Astronomical Journal, **108**, 1163-1177.

[5] Böttcher, M., et al. 2008, "*Relativistic Jets From Active Galactic Nuclei,*" WILEY-VCH Verlag GmbH & Co.KGaA, **230**

[6] Robert, J.G. and Gerald, S. 1996, "*Opacity of the Universe to High-Energy photons*," Physical Review Letters, **16**,252.

[7] American Association of Variable Star Observers 2010 '*Markarian 421*,' Retrieved December 24, 2018. Website: https://www.aavso.org/vsots_mark421

[8] Gilbert, V., Jean-Luc, A. 2009, "*Gamma-Ray Burst The Brightest Explosion in The Universe*," Springer Praxis Books Astronomy and Planetary Sciences.

[9] Liu, F.K., Liu, B.F., and Xie, G.Z. 1997, *"The Long-term Optical Behavior of MKN 421,"* Astronomy and Astrophysics Supplement Series, **123**, 569-574.

[10] Wei, C. 2004, "*X-Ray Flaring Activity of Markarian 421*," Department of Physics, Purdue University, West Lafayette, IN 47907

[11] Blazejowski, M., et al. 2005, "*A Structured Leptonic Jet Model of the "Orphan" TeV Gamma-Ray Flares in TeV Blazars,*" Astrophysics Journal. **630**, 130.

[12] Sarira, S., et al. 2018, "*The Origin of Multi-TeV Flares from The Nearest Blazar Markarian 421,*" The European Physical Journal. **78**, 557.

[13] H.E.S.S. Collaboration, et al. 2017, "*Gamma-ray blazar spectra with H.E.S.S. II mono analysis: The case of PKS 2155*-304 and PG 1553+113, Astrophysical Journal. **600**, A8.

[14] Cornils, M., Gillessen, E. 2003, "*The Optical System of The H.E.S.S. Imaging Atmospheric Cherenkov Telescopes. Part I: Mirror Alignment and Point Spread Function,*" Astropaticle Physics **20**, 129.

[15] Vincent, P., et al. 2003, "*Performance of the H.E.S.S. cameras,*" Proc. 28th International Cosmic Ray Conference (ICRC), 2887.

[16] Funk, S., Herman, G., Hinton J., et al. 2004, "*The Trigger System of The H.E.S.S. Telescope Array,*" Astroparticle Physics **22**, 285.

[17] Aharonian, F., et al. 2006, "*Observations of The Crab Nebula With HESS,*" Astronomy & Astrophysics **457**, 899.

[18] Li, T., & Ma, T. 1983, "*Analysis Methods for Results in Gamma-ray Astronomy*" Astrophysical Journal **272**, 317.

[19] McCarthy, D.D. 1998, "*The Julian and Modified Julian Dates*", Journal of the History of Astronomy **29**, 327.

[20] Maraschi et al. 1994, "*The 1993 multiwavelength campaign on 3C 279: The radio to gamma-ray energy distribution in low state,"* Astrophysical Journal, **435**, 93.

[21] H.E.S.S. Collaboration 2016, "*High Energy Stereoscopic System*," Retrieved August 22, 2017 from the H.E.S.S. website: https://www.mpi-hd.mpg.de/hfm/HESS/pages/about/

[22] Giomi, P. and Colafrancesco, S. 2006, "*Non-thermal Cosmic Backgrounds and prospects for future high-energy observations of blazars*," Experimental Astronomy **20**, 31-40.

[23] Biteau, J. 2013, "*A window on stochastic processes and gamma-ray cosmology through spectral and temporal studies of AGN observed with H.E.S.S.*," Laboratoire Leprine Ringuet, Ecole Polytechnique.

[24] Klepser, S., et al. 2017, "*Hadware and Software architecture of the upgraded H.E.S.S. camera*," PoS (ICRC2017) 834.

[25] Bonnefoy, S., et al. 2017, "*Performance of the upgraded H.E.S.S. cameras*," PoS (ICRC2017) 35.

[26] Aharonian, F., Akhperjanian, A.G., Anton, G., et al., 2009, "*Spectrum and variability of the Galactic center VHE gamma-ray source HESS J1745-290*," H.E.S.S. Collaboration, Astronomy & Astrophysics, **503**, 817.

[27] Ohm, S., et al. 2009, *"Gamma hadron separation in very-high-energy gamma-ray astronomy using a multivariate analysis method*" Astroparticle Physics **31**, 383-391.